Mechanisms of fault mirror formation and fault healing in carbonate rocks

Markus Ohl [a],*, Oliver Plümper [a], Vasileios Chatzaras [b], David Wallis [a], Christian Vollmer [c], Martyn Drury [a]

[a] *Department of Earth Sciences, Utrecht University, Princetonlaan 8a, 3584 CB, Utrecht, the Netherlands*
[b] *School of Geosciences, The University of Sydney, Sydney NSW 2006, Australia*
[c] *Institut für Mineralogie, Westfälische Wilhelms-Universität, Corrensstraße 24, 48149 Münster, Germany*

ABSTRACT

The development of smooth, mirror-like surfaces provides insight into the mechanical behaviour of crustal faults during the seismic cycle. To determine the thermo-chemical mechanisms of fault mirror formation, we investigated carbonate fault systems in seismically active areas of central Greece. Using multi-scale electron microscopy combined with Raman and electron energy loss spectroscopy, we show that fault mirror surfaces do not always develop from nanogranular volumes. The microstructural observations indicate that decarbonation is the transformation process that leads to the formation of smooth surface coatings in the faults studied here. Piercement structures on top of the fault surfaces indicate calcite decarbonation, producing CO_2 and lime (CaO). Lime subsequently reacts to portlandite ($Ca(OH)_2$) under hydrous conditions. Nanoscale imaging and electron diffraction reveal a thin coating of a non-crystalline material sporadically mixed with nano-clay, forming a complex-composite material that smooths the slip surface. Spectroscopic analyses reveal that the thin coating is non-crystalline carbon. We suggest that ordering (hybridisation) of amorphous carbon led to the formation of partly-hybridised amorphous carbon but did not reach full graphitisation. Calcite nanograins, <50 nm in diameter, are spatially associated with the carbon and indicate that the decomposition products acted as a crystallisation medium. Within this medium, portlandite back-reacted with CO_2 to form nanocrystalline calcite. Consequently, two types of calcite nanograins are present: nanograins formed by grain-size reduction (primary nanograins, >100 nm) and new nanograins formed by back-reaction (secondary nanograins, <50 nm). Hence, we suggest that the new, secondary nanograins are not the result of comminution during slip but originate from pseudomorphic replacement of calcite after portlandite. The continuous coverage of partly-hybridised amorphous carbon on all samples suggests that calcite decarbonation products may develop across the entire fault surface, controlling the formation of carbonate fault mirrors, and may facilitate slip on a decarbonation-product glide film.

© 2019 Elsevier B.V. All rights reserved.

1. Introduction

Brittle deformation of upper-crustal rocks can result in high-magnitude seismic events (Scholz, 1998). Mirror slip surfaces (MSSs) along principal slip zones in carbonate rocks provide an excellent opportunity to investigate the deformation processes that occur in relation to slip events in the seismogenic zone. Carbonate-hosted faults can produce seismic events with magnitudes of $M_w = 6$ and greater. These events present a hazard to populated regions, such as the Mediterranean. The defining feature of MSSs is the high degree of visible-light reflectance resulting from a low surface roughness. MSSs can form at seismic slip velocities and, therefore, may indicate paleo-seismicity (Siman-Tov et al., 2013; Smith et al., 2013; Fondriest et al., 2013; Kirkpatrick et al., 2013; Spagnuolo et al., 2015). However, MSS have also been developed at sub-seismic slip conditions in deformation experiments (Tisato et al., 2012; Verberne et al., 2014) and, thus, they are not necessarily diagnostic of seismic slip.

The studies from Siman-Tov et al. (2013), Collettini et al. (2014) and Verberne et al. (2014) suggest that the low surface roughness of MMS may be the result of nano-sized grains (<1 μm), which constitute the uppermost layers of many principal slip surfaces. However, work by Fondriest et al. (2013) demonstrates that truncated, large grains can be part of mirror surfaces as well, il-
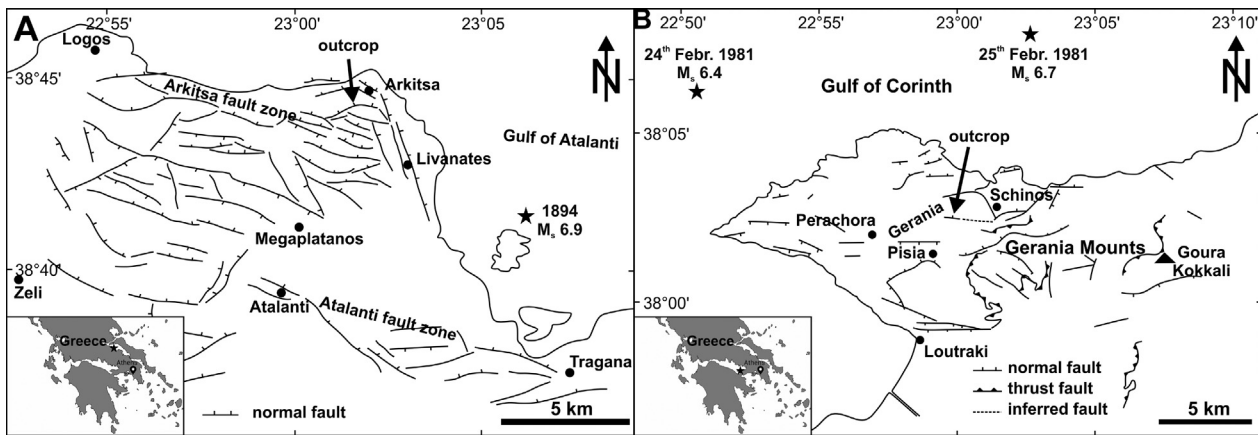
Fig. 1. Tectonic maps of the study areas. Insets show the geographical location within central Greece. **A:** Location of the studied exposure of the Arkitsa fault zone (modified after Jones et al., 2009; earthquake data: NOAA). **B:** Outcrop location of the Schinos fault segment north of Corinth (modified after Kaplanis et al., 2013 and Collier et al., 1998).

lustrating that the formation of ultra-polished surfaces does not necessitate a nanograin coating along the slip surface. In addition, nanogranular coatings are also produced in deformation experiments under seismic conditions (Green et al., 2015; Spagnuolo et al., 2015). Therefore, the formation of natural MSSs has been associated with the development of a nanogranular slip-surface coating during seismic events. These nanogranular coatings may in addition control the frictional behaviour of the fault (Han et al., 2007a, 2007b; Han et al., 2010; Di Toro et al., 2011; Bullock et al., 2014; De Paola et al., 2015; Smeraglia et al., 2017).

Current research suggests different formation mechanisms for carbonate mirror slip surfaces: (1) Formation of elongate, twin-derived beams by plasticity and subsequent brittle fracturing of the beams to form a nanograin coating (Siman-Tov et al., 2013) and (2) localised dynamic recrystallisation and static recrystallisation (Smith et al., 2013). Several studies have reported decarbonation products during or after experiments that produced fault mirrors (Han et al., 2007a and 2007b, De Paola et al., 2011; Smith et al., 2013; Fondriest et al., 2013, Delle Piane et al., 2017). Pluymakers and Røyne (2017) found an increase in nanospherules (nanoparticles) responsible for reducing the surface roughness after heating, which demonstrates that existing mirror slip surfaces could be affected by heating events. These studies suggest that the formation of nanograins and fault mirrors are intrinsically linked, tying the formation of mirror slip surfaces to the formation of nanograins.

One of the main mechanisms of fault-gouge formation is grain-size reduction by comminution. Reduction of grain size commences by inducing fractures at grain-to-grain contacts, which then break the grains. The grain-size dependence of the modified Hall-Petch relation proposed by Sammis and Ben-Zion (2008) illustrates that smaller grains require higher differential stresses to fracture. Therefore, local stress concentrations during co-seismic events may be favourable sites for the generation of nanograins by fracturing micron to millimetre-sized grains. Because of the high stress concentrations during earthquakes, nanograins may be evidence for paleo-seismic events.

Less commonly considered effects of fault-rock deformation in carbonates are thermo-mechanical processes, e.g. decarbonation. Products of decarbonation processes are reported from experiments (Han et al., 2007a and 2007b; De Paola et al., 2011; Verberne et al., 2014; Spagnuolo et al., 2015; Delle Piane et al., 2017) and from natural faults (Vigano et al., 2011; Collettini et al., 2013). The experimental studies of Verberne et al. (2014), Spagnuolo et al. (2015) and Delle Piane et al. (2017) report the presence of amorphous carbon as a deformation product, and

Han et al. (2007a) mention the presence of portlandite ($Ca(OH)_2$). Some natural faults also exhibit amorphous glass coatings around euhedral calcite crystals in potential carbonate pseudotachylites (Vigano et al., 2011). In addition, deformation experiments on silicates (Yund et al., 1990; Di Toro et al., 2004; Pec et al., 2012; Hirose et al., 2012; Toy et al., 2015) produce non-crystalline or partly-amorphous silicate materials (Pec et al., 2012).

We investigated the surface and the underlying few tens of micrometres of two natural carbonate fault-mirror structures to test the hypothesis of a nanogranular surface coating. Our high-resolution electron microscopy and Raman spectroscopy analyses demonstrate that a thin coating of decarbonation products is able to produce a MMS without a nanogranular surface coating, similar to the results of Fondriest et al. (2013). In addition, we suggest that the amorphous products may facilitate and lubricate seismic slip (De Paola et al., 2011; Di Toro et al., 2011) while being produced or possibly re-strengthen the fault by post-seismic recrystallisation of the decomposition products during the inter-seismic period.

2. Geological setting

2.1. Geology of the Arkitsa fault zone

The 700 m long Arkitsa fault surface exposure (Fig. 1A) belongs to the Kamena Vourla fault system; a northward-dipping, ESE-WNW striking, active normal fault zone of approximately 50 km length along the southern coast of the Gulf of Evia. This left-stepping fault system consists of the Kamena Vourla, the Agios Konstantinos and the Arkitsa fault segments (Roberts and Jackson, 1991; Ganas et al., 1998). The study area (38°43′56.17″N, 23°0′27.41″E) is situated within the Pelagonian zone of Central Greece. In general, the Arkitsa fault planes juxtapose Late Triassic to Middle/Late Jurassic platform carbonates in the footwall with lower Pliocene-Pleistocene to Quaternary sediments in the hanging wall (Kokkalas et al., 2007). The Arkitsa fault scarp itself is an anthropogenically formed fault exposure first described by Jackson and McKenzie (1999). Quarrying for two decades removed a major part of the hanging-wall colluvium to reveal three large, smooth fault planes of up to 65 m height (Kokkalas et al., 2007).

Historical records of seismicity in the Gulf of Evia area indicate about 13 rupture events from 426 BC until the last major event in 1894 (Ganas et al., 1998; Ganas et al., 2006), with a magnitude M_s 6.9 earthquake hosted within the Atalanti fault zone (Fig. 1A) (Ambraseys and Jackson, 1990). This number of events fits with the approximately 50 slip increments identified by Jackson and

McKenzie (1999), where the authors calculated the slip increments from fault plane height and average earthquake slip distances. Evidence for Holocene seismic activity along the Arkitsa fault planes is recorded by the approximately 1 m unweathered fault scarp existing prior to quarrying (Jones et al., 2009).

2.2. Geology of the Schinos fault zone

The Schinos fault zone is located north-east of Corinth within the Gerania mountains, with the studied exposure (38°2′14.40″N, 23°0′22.33″E) belonging to the Gerania unit of the Internal Hellenides (Kaplanis et al., 2013). Formation of the 120 m long fault exposure is from material excavation for the adjacent dirt road. The fault plane is an east-west striking, northward-dipping normal fault plane hosted within Upper Triassic limestones and dolomites. The stratigraphic succession of the Gerania unit includes from bottom to top: Permian sedimentary and volcanic rocks, Upper Triassic neritic limestones and dolomites, Lower Jurassic limestones, an Upper Jurassic succession of rift-related sediments overlain by either Ammonitico Rosso (Bathonian or Oxfordian age) or radiolarian sediments, and ophiolite-derived turbidites of the Beotian flysch (Kaplanis et al., 2013).

Seismicity data record an earthquake sequence in the Corinth region with three main shocks: 24th February, 1981, M_s 6.7; 25th February, 1981, M_s 6.4 and 4th March, 1981, M_s 6.4 (Collier et al., 1998). Based on the epicentral location and a mismatch between the focal mechanism, Collier et al. (1998) interpreted that the 24th February event started with displacement on an offshore fault and continued to rupture the Pisia fault, producing a surface break. In addition, Collier et al. (1998) propose the same succession of events for the 25th February event, which caused a displacement on the Schinos fault, probably forming the most recent event on the fault plane that we study here.

3. Methods

We analysed drill-core samples from the Arkitsa and Schinos fault exposures using a range of micro-analytical techniques. In total, 40 drill cores, 2.54 cm in diameter, were collected from the Arkitsa fault zone and, 18 were collected from the Schinos fault zone. The maximum retrievable drill-core lengths did not exceed 10 cm (Arkitsa) and 5 cm (Schinos) as the porosity of the fault rock increases, and the material loses its cohesion with distance from the fault surfaces. Seven samples from the Arkitsa fault zone and four samples from the Schinos fault zone were chosen for further investigation based on the best-preserved mirror surfaces. Sample cores were sputter coated with an 8-nm thick layer of platinum/palladium for charge deduction.

From both faults, two representative samples were selected for electron-transparent foil preparation using a FEI Helios Nanolab G3 Dualbeam focused ion beam scanning electron microscope (FIB-SEM). Prior to ion beam deposition of the main platinum strip, a 200-nm layer of platinum was deposited using the electron beam (2 kV, 0.4 nA) to prevent surface amorphisation by the ion beam as a preparation artefact. Transmission electron microscope (TEM) investigations of the foils were carried out with a FEI Talos F200X. TEM images were acquired with 200 kV acceleration voltage and 5 nA or 10 nA beam current depending on final sample thickness. The FEI Talos SuperEDX detector was used for chemical element mapping via energy dispersive X-rays (EDX) in scanning transmission electron microscope (STEM) mode. EDX maps were quantified post-acquisition with Bruker Esprit 1.9 software using the Cliff-Lorimer approximation and ImageJ.

Electron energy loss spectroscopy (EELS) data were acquired with a Zeiss Libra 200FE in TEM mode at 200 kV with an Omega in-column energy filter. The energy resolution of EELS analyses was 0.7 eV, measured at the full width half maximum (FWHM) of the zero-loss peak. Energy loss spectra were obtained at 250,000× magnification with a 100 μm filter-entrance aperture giving an effective aperture of about 40 nm on the sample. The convergence angle of EELS was about 0.1 milliradian (mrad), and the acceptance angle was defined by the 60 μm diameter of the objective aperture giving a collection angle of 11.6 mrad. Measurement times of EEL spectra were set to 1–5 s, with 5–10 frames/spectrum, on a slow-scan CCD (model UltraScan 4000), with binning of 4×4 pixels (giving 1024 pixels), and an energy spread of 0.08 eV/pixel, resulting in an energy range of 82 eV in the acquired spectra. Spectra were deconvolved with the zero-loss peak to remove the effect of plural scattering and background-subtracted assuming a power law function with Gatan´s Digital Micrograph software.

Raman spectroscopy was carried out with a WiTec ALPHA300 R confocal microscope to identify and characterize possible reaction or decomposition products on the fault surfaces. We used a laser with a wavelength of 532 nm and a spectral grating of 600 grooves/cm. Data acquisition, data post-processing and peak fitting were performed with WiTec ProjectFour 4.1 software and Fityk 0.98 (Wojdyr, 2010) peak fitting software. In accordance with (Ferrari and Robertson, 2000) we determined the intensity ratios of the D to G peak, $\frac{I(D)}{I(G)}$, to obtain information about the degree of crystallinity within carbon phases. We used the approach by Ferrari and Robertson (2000) based on first principle considerations to determine the peak height ratios because the information about the less disordered aromatic rings and the clustering of the sp^2 phase is contained in the intensity maximum of the D peak and not in the width. Surface roughness measurements were executed within a Nanoscope atomic force microscope (AFM). Calculation of reaction enthalpy values were executed with SUPCRT92 (Johnson et al., 1992) at standard conditions (1 bar, 298 K).

4. Results

4.1. Field results

The exposed surface of the Arkitsa fault (Fig. 2A) exhibits a range of slip-related structures. At outcrop scale, the fault plane exposure steps over, which suggests the presence of several slip planes inside the fault damage zone. The fault surface contains pronounced slip grooves parallel to the direction of oblique slip. Fractures with a spacing on the order of one metre are oriented approximately perpendicular to the grooves (Fig. 2A). Parts of the slip plane are covered with residual reddish-brown hanging-wall breccia, incorporating fragments of dark host-rock carbonate up to several decimetres in size (Fig. 2A). The most prominent feature is the low roughness of the fault surface, which enables the reflection of sunlight (Fig. 2B). The fault rock is a matrix-supported, greyish cataclasite with dark carbonate clasts up to several centimetres in size (Fig. 2C). Slip-parallel alignment of clasts on the fault surfaces can be traced over several meters (Fig. 2C).

The Schinos fault surface (Fig. 2D) exhibits a range of structures formed during slip. We observe stepovers, indicating the presence of several fault planes inside the fault damage zone. The fault surface is extremely smooth with areas not only reflecting light but also mirroring the surrounding vegetation (Fig. 2E). Fragments of grey carbonate host rock are incorporated into the red-orange footwall cataclasite. The clasts are strongly aligned in the slip direction and usually do not exceed 1–2 cm in size (Fig. 2F). The fault surface contains pronounced slip grooves and a wavy surface morphology (Fig. 2D). The mirror surfaces of both faults are hosted inside a zone of high competence with average thicknesses of 10 cm and 5 cm for the Arkitsa and Schinos faults, respectively.
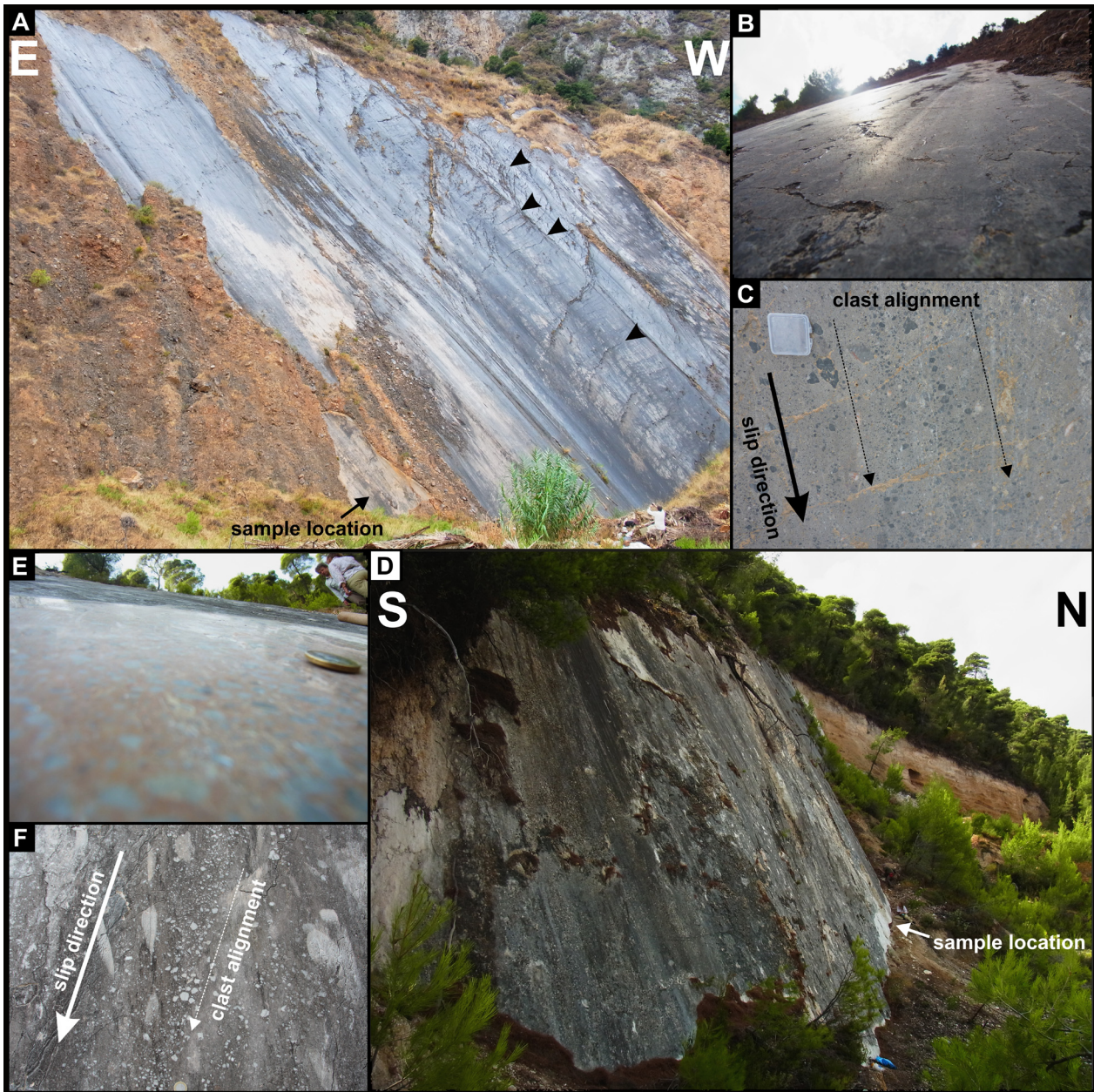
Fig. 2. Representative field structures from Arkitsa (A–C) and Schinos (D–F) fault exposures. **A:** Overview of Arkitsa fault exposure showing one of the three main slip planes with reddish-brown hanging-wall breccia cover on part of the slip surface. Black arrows indicate fractures perpendicular to slip direction. Person for scale, bottom right corner. **B:** Fault surface reflecting sunlight. **C:** Alignment of host rock fragments parallel to slip direction. Box approx. 5×4 cm. **D:** Schinos fault surface exposure shows grey weathering of the slip plane. The slip plane is curved with the salient pointing out of the figure. Fault scarp to the north is now covered by alluvium. **E:** Image demonstrating fault surface reflectivity. Reflection of vegetation along the top edge and above the one-euro coin. **F:** Grey, weathered fault plane showing a strong alignment of light grey host-rock clasts parallel to slip direction (one-euro coin for scale, bottom edge).

4.2. Slip surface microstructures

SEM analyses of the Arkitsa and Schinos slip surfaces reveal a low surface roughness at the microscale. The surfaces are well polished and, in some places, preserve parts of the hanging wall (Fig. 3A and F). Microgrooves are aligned parallel to the slip direction (Fig. 3B), and holes with a diameter of 6–8 μm pierce the slip surfaces (Fig. 3A and D). The average surface roughness measured by AFM is 63.5 nm for the Arkitsa fault surface and 32.3 nm for the Schinos fault, respectively (see SF1 in the supplementary material). Localized erosion of the Arkitsa slip surface exposes the underlying fault rock, with a grain size of 2–5 μm (Fig. 3A, B and C). The first 10–20 μm of the fault rock below the Arkitsa slip surface consist of a fine-grained deformation product, which is situated on top of a comparatively coarse-grained, less deformed material (Fig. 3B and C).

In contrast, the Schinos fault surface consists of large, truncated grains with boundaries that meet in triple junctions (Fig. 3D and inset). A fragmented layer lies on top of undeformed calcite crystals (Fig. 3E), and the damage extends about 10–20 μm into the fault rock. Here also an amorphous material is present on the slip plane (Fig. 3E and F). On both faults, Arkitsa and Schinos, the amorphous material has a low contrast in backscattered-electron images (Fig. 4A and B). The phase also coats grain edges and reduces the slip surface roughness (Fig. 3C, E and F). In addition, the amorphous material infiltrates interstitial regions of the hanging-wall breccia and holds residual pieces of hanging wall in place (Fig. 3F).
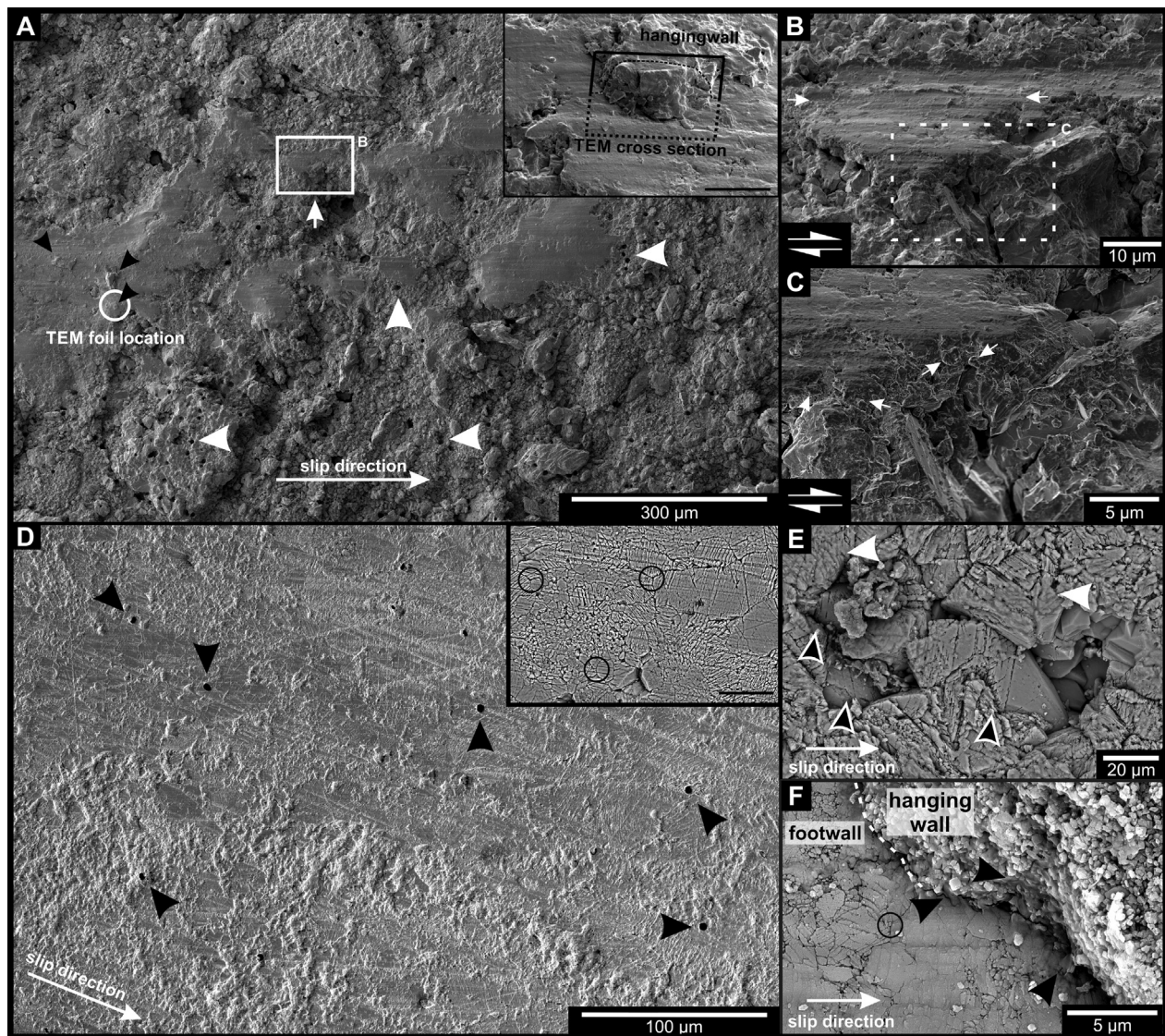
Fig. 3. Representative slip surface microstructures of the Arkitsa (A–C-) and Schinos (D–F) exposures. **A:** Secondary electron overview image of the Arkitsa slip surface. Smooth slip patches with microgrooves parallel to slip direction. Uniform holes (white arrows) penetrate the slip surface. Residue of hanging wall on top of the slip surface patch (black arrows, white circle) with TEM sample location. Inset: Detailed view of TEM foil location from Fig. 5A, white circle. Scale bar = 5 μm. **B:** Close-up of slip surface from A. Fine-grained slip surface material situated on top of coarse fault rock grains. Microscope stage tilted to 52°. **C:** Close-up of section from B. Amorphous material covers roundish grains (*black arrows*). **D:** Secondary electron image of Schinos slip surface with microgrooves parallel to slip direction. Uniform holes penetrate the principal slip surface (black arrows). Inset: Backscatter electron image illustrating triple junction grain boundary contacts. Scale bar = 50 μm. **E:** Backscatter electron image top view onto the slip surface. Cracks in idiomorphic calcite crystals are visible a few micrometres into the crystal (black-white arrows). Amorphous material with low backscatter contrast covers parts of the slip surface and reduces surface roughness (white, dashed lasso) **F:** Backscatter electron image of the contact between footwall and hanging wall (dashed line). Black arrows indicate the locations of an amorphous material with lower backscatter contrast. Black circle shows grain boundary triple junction.

Fig. 4 presents Raman spectra from the amorphous material. Two broad peaks between 1200–1700 cm^{-1} indicate the presence of a disordered carbon phase, whilst a peak at 1086 cm^{-1} demonstrates the presence of crystalline calcite. The fitted spectrum from the Arkitsa fault plane gives a $\frac{I(D)}{I(G)}$ ratio of 0.543 at a D-peak position of 1339 cm^{-1} and a G-peak position of 1584 cm^{-1}. The fitted spectrum from the Schinos fault plane gives a $\frac{I(D)}{I(G)}$ ratio of 0.789 at a D-peak position of 1344 cm^{-1} and a G peak position of 1587 cm^{-1}.

4.3. Nanostructures

TEM analyses on FIB-SEM foils of both fault-surface exposures reveal a thin surface coating (e.g. Fig. 8A and F, but also Fig. 6A–D). The uppermost layer of both fault-rock exposures is defined by a principal slip surface with a thin, non-crystalline coating between hanging wall and footwall (Fig. 5A and B, Fig. 6A–D). The coating exhibits homogenous diffraction contrast, shows no lattice fringes (Fig. 6A to D, 8A and F), and EDX analyses indicate the presence of carbon (C), iron (Fe), silicon (Si) and aluminium (Al) (Fig. 7, Si content of Arkitsa ∼40 area % estimated with ImageJ). A similar content of impurity elements has been mentioned by Pluymakers and Røyne (2017), Collettini et al. (2013) and Goldberg et al. (2016). The coating connects hanging-wall breccia with the footwall fault surface (Fig. 6B and D) but also extends into the hanging-wall breccia (Fig. 6A and C). EELS measurements of the amorphous material are given in the inset of Fig. 6D. The onset of the π^* peak represents the measured carbon K-edge at 284 eV, which is followed by a 'whaleback-shaped' σ^* region. In addition, the measurement of the Schinos sample exhibits an additional peak at 286.5 eV, possibly indicating C–O bonding.
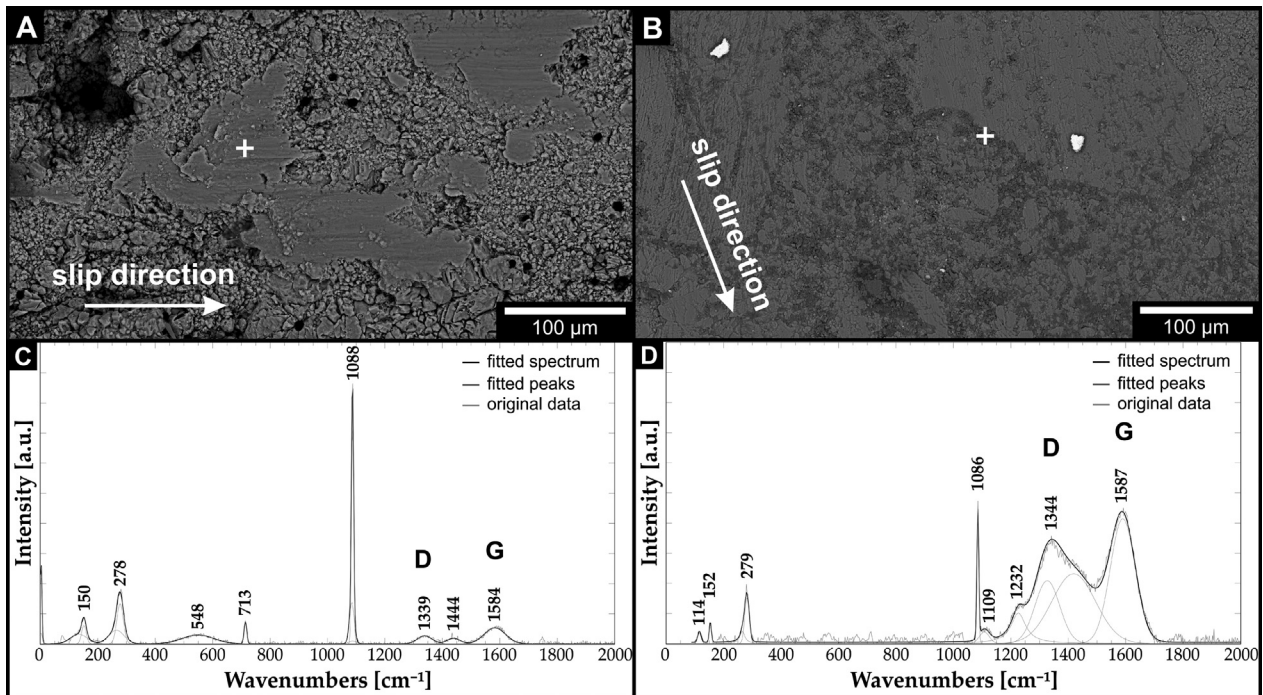
Fig. 4. Backscatter electron images with locations of Raman spectroscopy measurements for Arkitsa (A and C) and Schinos (B and D) slip surfaces. **A and B:** Backscatter electron images of the fault surfaces. A phase with low backscatter contrast (darker grey) is visible in B. **C and D:** Raman spectra showing the D and G peak position of a disordered carbon phase.

We observe a direct relation between the spatial distribution of amorphous material and calcite nanograins. For the Arkitsa fault exposure, a nanogranular layer is present with rounded, elliptical calcite nanograins of ∼50 nm size between the footwall and the hanging-wall breccia (Fig. 5A, 6A, B and 7). Selected area electron diffraction (SAED) patterns of the Arkitsa nanogranular layer in Fig. 5A demonstrate the polycrystalline nature of the material with clustered diffraction spots forming two arcs subtending an angle of about 75° (inset Fig. 6A). Fig. 8A reveals that the thickness of the coating varies along the slip surface and locally incorporates calcite grains from the underlying nanostructure. We find that calcite nanograins are not restricted to the principal slip surface but also occur away from the displacement zone inside the fault rock (Fig. 8B). The nanograins do not contain any dislocations (Fig. 6B and 8B) and are not always in grain-to-grain contact in the plane of the section. Calcite nanograins of the Schinos exposure are mostly located between large grains along the principal slip surface (Fig. 8C and D). The gaps between large grains also contain an amorphous material that increases the overall smoothness of the fault surface. Inside the amorphous material, most nanograins have elongate shapes with no dislocation substructure (Fig. 8D). Nano-clay minerals often wrap around the calcite nanograins (Fig. 8D).

Further TEM investigation of the slip surfaces reveals a variety of slip-derived deformation nanostructures. Neither fault exposure exhibits a gradual decrease in grain size towards the slip surface, but both show an abrupt change instead. Adjacent to the principal slip surface, we observe twinned calcite crystals about 2–5 μm in size (Fig. 5A and B). Dislocations are homogeneously distributed in the larger crystals from the Arkitsa exposure (Fig. 5A). For the Schinos case, the dislocation distribution appears to be less ordered, with dislocations concentrated towards grain contacts in slip direction (Fig. 8C). Bent cleavage fractures dip down from the Arkitsa slip surface and exhibit minor displacements together with slight increases in dislocation density along fracture planes (Fig. 5A and 6A). Along the slip surface, the nanostructure of the Arkitsa fault varies in intensity and develops a foam nanostructure (Fig. 8A).

The layer thickness of the foam nanostructure is about 1 μm and the grain size ranges from 100–200 nm with the grain boundaries exhibiting triple junctions at ∼120° angles (Fig. 8A). This nanostructure is not observed in the samples analysed from the Schinos exposure, which instead contain dislocation arrays (Fig. 8C and E). In general, the foam nanostructure at Arkitsa appears to be less developed adjacent to the slip surface, especially where the fracture density is highest.

5. Discussion

5.1. Processes revealed by nano/microstructures

5.1.1. Decarbonation and carbon reduction

Nanostructural investigation of the Arkitsa and Schinos fault exposures reveal the importance of calcite decarbonation products for the formation of a smooth fault surface. TEM images reveal a coating of an amorphous material. We suggest that the amorphous material formed following calcite decarbonation, as a result of shear heating at asperity contacts or alternatively, the 'severe' introduction of dislocations during fault slip. In our natural samples, holes piercing the principal slip surface (Fig. 3A and D) indicate CO_2 degassing as a product of the decarbonation reaction

$$CaCO_{3(s)} \rightleftharpoons CO_{2(g)} + CaO_{(s)} \quad \left(\Delta H^0_{298\,K} = +178\,\text{kJ}\,\text{mol}^{-1}\right) \quad (1)$$
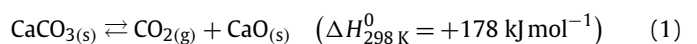
reported to occur due to thermal decomposition of calcite starting at 600 °C (Rodriguez-Navarro et al., 2009). However, experiments by Martinelli and Plescia (2004) recorded CO_2 emission during ball milling experiments of calcite without increasing the macroscopic temperature. In addition to the CO_2 emissions, the authors detected the presence of amorphous lime (CaO) in their milling product as a result of a process termed 'mechanical liming'. Subsequent heating of the milling product resulted in a decrease of amorphous lime and the formation of calcite. The heating of the milling product carbonates the lime with atmospheric CO_2 after overcoming the activation energy of reaction (1), leading to the
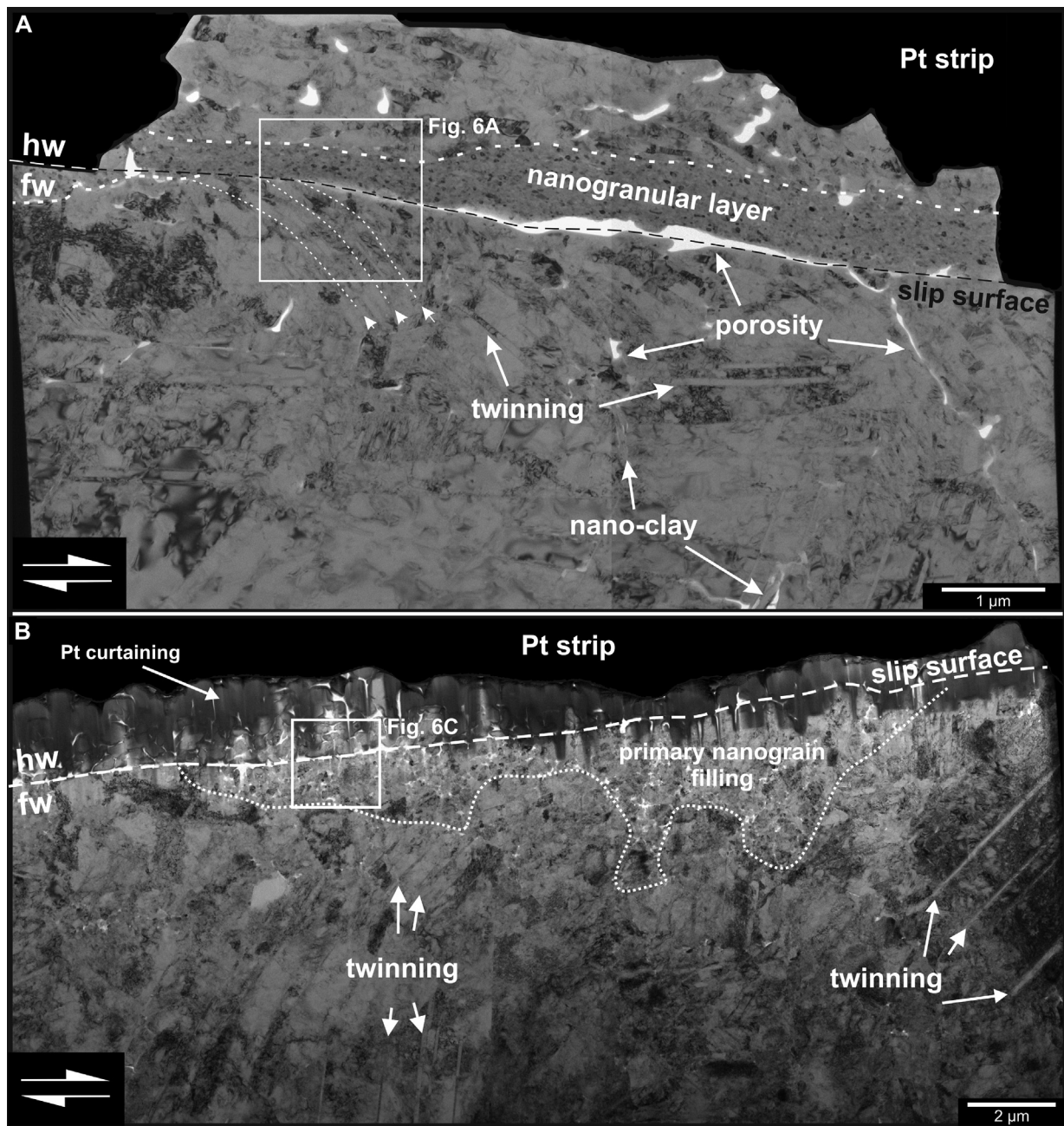
Fig. 5. Overview of TEM cross sections into the principal slip surfaces of Arkitsa and Schinos, including preserved hanging-wall residue. **A:** Bright-field TEM image overview of representative Arkitsa nanostructures. The hanging-wall breccia consists of small, elongated calcite fragments held in place by non-crystalline carbon. The nanogranular layer is part of the hanging-wall breccia and lies on top of deformed calcite crystals. Fractures (dashed lines) bend down from the principal slip surface into the deformed calcite crystals. Fractures and holes form porosity inside the mirror slip volume and are filled either with non-crystalline carbon and/or nano-clay (see arrows with labelling). **B:** Bright-field TEM image with representative Schinos nanostructural hanging-wall to footwall relation. The hanging wall consists of small grains of several hundred nanometres. Individual grains are surrounded by non-crystalline carbon. The footwall hosts a discontinuous, primary nanograin filling. The grain size increases abruptly with distance from the slip surface to grains of several micrometres in size. Larger grains contain twins. hw = hanging wall, fw = footwall.

formation of new calcite. The experiments of Martinelli and Plescia (2004) demonstrate that reaction (1) can also take place just by deforming calcite without reaching macroscopic temperatures >600 °C, although the temperature at asperity contacts could be higher. Mechanical liming may be important for wet deformation conditions where fluids are present and will buffer the temperature increase until all fluid of the system transforms into vapor. The buffering of temperature during deformation is in agreement with observations by Demurtas et al. (2019), where temperatures of <200 °C were recorded during water-damped experiments at seismic velocities. In contrast, the same study records temperatures

of >600 °C for experiments at room humidity. We suggest that decarbonation can occur at macroscopic temperatures <600 °C by mechanical liming, even under wet conditions, leading to the formation of lime and CO_2.
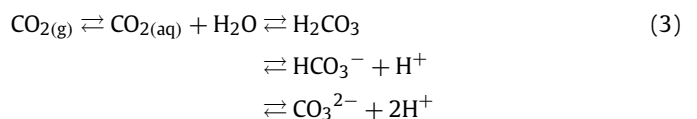
The acquired electron energy loss and Raman spectra indicate the presence of a carbon phase. Hence, the presence of this phase implies the occurrence of carbon-reducing processes because reaction (1) does not produce elemental carbon. Precipitation of carbon in deformation experiments of Oohashi et al. (2014) under a hydrogen atmosphere suggests that the reaction
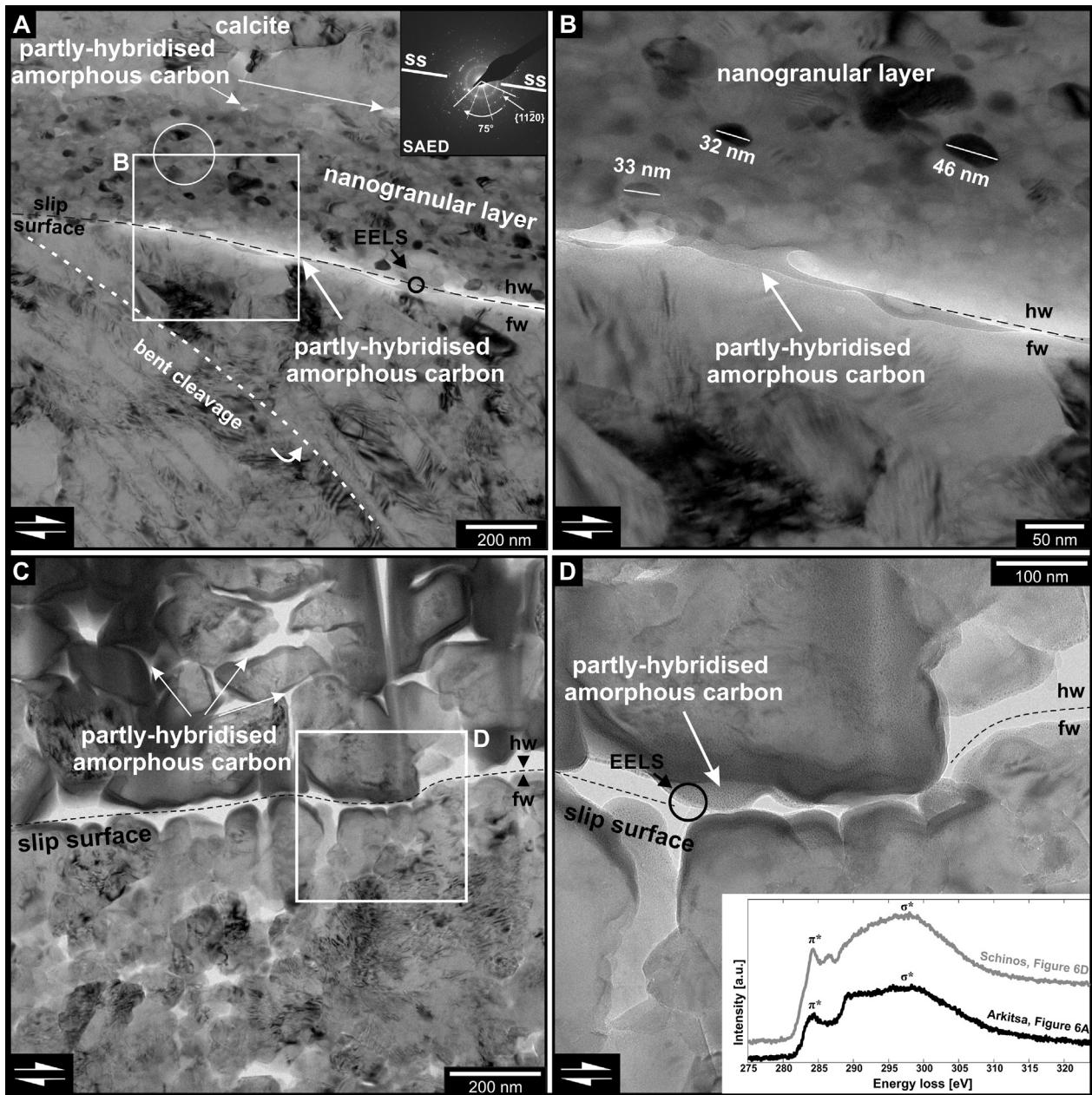
Fig. 6. TEM cross sections illustrating the relationship between hanging-wall (*hw*) breccia and footwall (*fw*) contact for Arkitsa (A–B) and Schinos (C–D). **A:** TEM bright field close-up from Fig. 5A. Non-crystalline carbon establishes the contact between hanging wall and footwall. The footwall consists of large, stressed calcite crystals with bent fractures. Nanogranular layer with non-crystalline carbon and calcite nanograins. White circle indicates SAED location (circle diameter = aperture diameter); black circle depicts EELS measurement (circle diameter = effective aperture diameter). Inset: SAED showing two sets of crystal orientation. ss = slip surface. **B:** TEM bright field close-up from A. Non-crystalline carbon connects hanging wall and footwall. The nanogranular layer produces Moiré fringes indicative of overlapping crystal lattices. Nanograins are not always in grain-to-grain contact. **C:** TEM bright field close-up image from Fig. 5B. The grain size of the hanging wall is 200 nm and larger. The grain size of the footwall directly at slip surface is about 100 nm. **D:** TEM bright field close-up image from C. The hanging wall and footwall are connected via non-crystalline carbon. Black circle depicts EELS measurement (circle diameter = effective aperture diameter). Inset shows EELS spectra from black circles in A and D.

$$CO_{2(g)} + 2H_{2(g)} \rightarrow C_{(s)} + 2H_2O_{(g)} \quad \left(\Delta H^0_{298\,K} = -90 \text{ kJ mol}^{-1} \right) \tag{2}$$
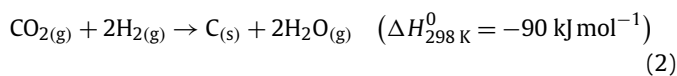
can reduce CO_2 to form carbon. Similarly, Spagnuolo et al. (2015) detected $H_{2(g)}$ and $CO_{2(g)}$ degassing during their experiments. Although reaction (2) is expressed as a chemical vapour deposition reaction, some of the hydrogen produced can go into solution to reduce dissolved CO_2. This process is known to occur in hydrothermal systems where dissolved hydrogen can interact with $CO_{2(aq)}$ to form reduced carbon phases (e.g., Milesi et al., 2015). Under wet conditions, the CO_2 from reaction (1) goes into solution starting the hydrolysis reaction

$$CO_{2(g)} \rightleftharpoons CO_{2(aq)} + H_2O \rightleftharpoons H_2CO_3 \tag{3}$$
$$\rightleftharpoons HCO_3^- + H^+$$
$$\rightleftharpoons CO_3^{2-} + 2H^+$$

to give carbonic acid, hydrogen carbonate, carbonate ions, and protons (Ruiz-Agudo et al., 2013). The mole fraction solubility (X_1) of CO_2 in water at room temperature is, with $X_1 = 6.15 \times 10^{-4}$, one order of magnitude larger than H_2 with $X_1 = 1.411 \times 10^{-5}$ (Gevantman, 2000). It is, therefore, more likely that a larger amount of CO_2 will dissolve in water and form carbonic acid, being the more probable proton donor for reducing carbon from the residual CO_2. As an alternative, CaO surfaces can act as potential
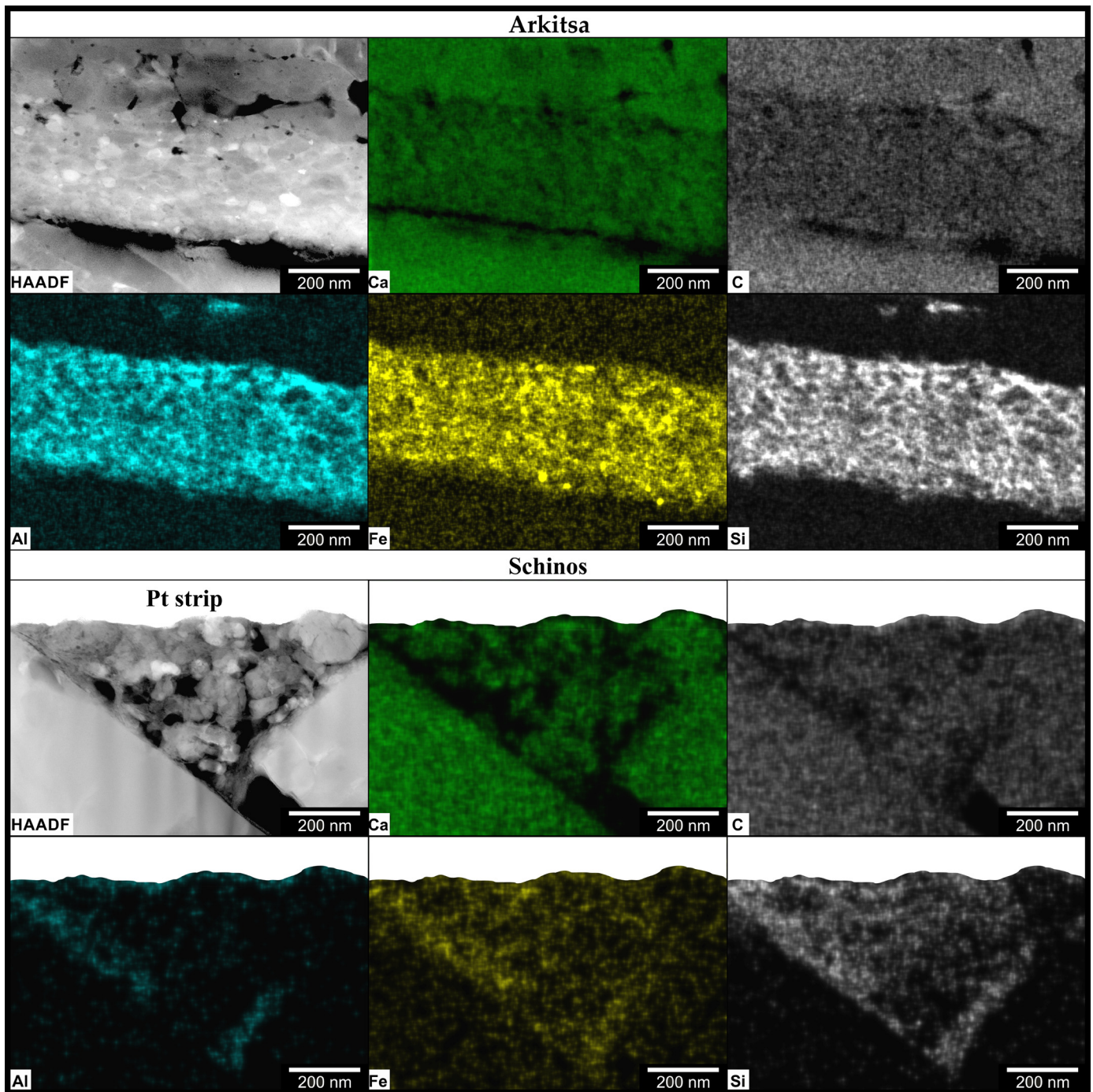
Fig. 7. TEM-EDX maps of calcite nanogranular layer from Fig. 5A (Arkitsa) and surface filling Fig. 8C (Schinos) visualizing the element distribution. Overlap of calcium (Ca) and carbon (C) distribution confirms that the grains inside are calcite. Aluminium (Al), iron (Fe) and silicon (Si) are concentrated in the interstitial region around the calcite grains.

catalytic sites and promote the reaction with H_2O at kinks, corners and/or steps. These surfaces can split H_2O leading to one hydroxyl ion (OH^-) and one proton (H^+) which in turn may also be able to reduce carbon from CO_2 (Kudłacz and Rodriguez-Navarro, 2014). The main requirement for this reaction to occur is the presence of crystalline CaO. This would either require prior crystallisation of the suspected amorphous lime from reaction (1) or the lime resulting from reaction (1) was already crystalline. Calcium ions (Ca^{2+}) decrease the pH of the water facilitating CO_2 solubility. Earth-alkali metal reactions with water are commonly known to produce hydrogen by reaction of the metal with water to form H_2 and the corresponding metal hydroxide. As the reduction of CO_2 by hydrogen does not require the participation of an additional reducing agent, it is likely to occur also under closed-system experimental conditions. With a variety of possible production reactions, it remains challenging to identify the main reaction responsible for the source of hydrogen for CO_2 reduction. However, a combination of several processes is likely, with the simplest being the hydrolysis of CO_2 in H_2O. The CaO or Ca^{2+} interaction with water can increase the pH up to 12.4, as shown in experiments by Ruiz-Agudo et al. (2013), which increases the solubility of CO_2 in water and would facilitate reaction (3). In general, the result would be the precipita-
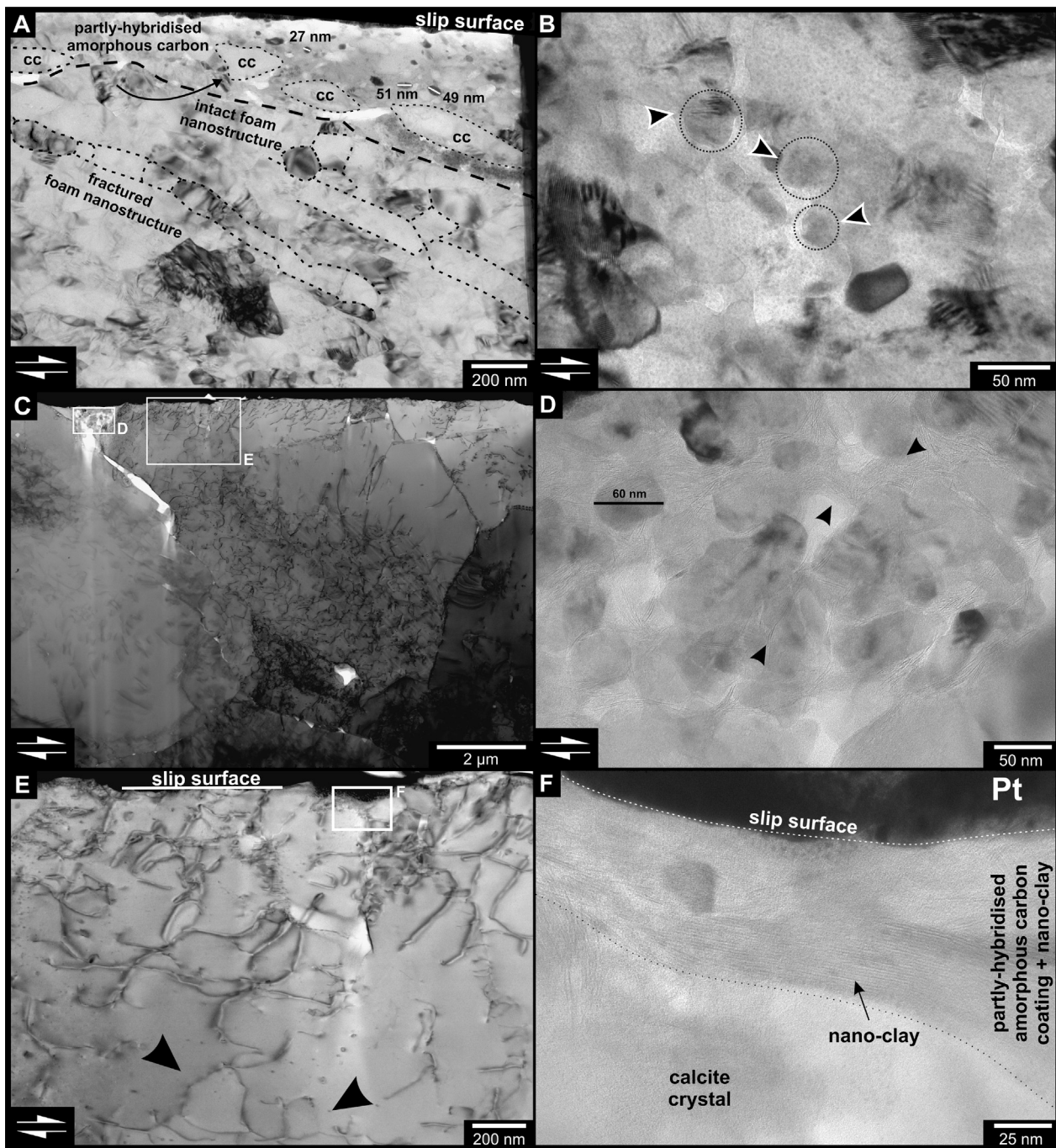
Fig. 8. Nanostructures of fault surface coating and nanograin abundance not associated with the principal slip surface. **A:** Bright-field TEM image from the Arkitsa exposure. Amorphous slip surface coating with calcite nanograins and crystal fragments from underlying foam nanostructure (black arrow). A sharp contact separates the underlying nanostructure from the slip surface coating. Nanostructure with former fracture planes (dashed lines), which originate from the principal slip surface, and overprint the existing nanostructure. **B:** Calcite nanograins away from the principal slip surface hosted inside non-crystalline carbon. Tip direction of black-white arrows indicate lattice fringe orientation of new grains. C: Bright-field STEM image overview. Large grains (5 μm) with a heterogeneous dislocation density distribution. **D:** Calcite nanograins in non-crystalline carbon as a filling between two grain boundaries directly at the principal slip surface. Clay minerals wrap around the nanograins (black arrows). **E:** Bright-field STEM close-up from C showing the dislocation structure directly at the principal slip surface. Black arrows point to frozen dislocation loops. **F:** Bright-field TEM image from the Schinos exposure. Amorphous slip surface coating mixed with nano-clay on top of calcite crystal. cc = calcite.

tion of carbon from the fluid, which would not be restricted to the principal slip surface but would also occur within existing porosity away from the slip surface.

5.1.2. Carbon-bond sp² hybridisation

The obtained $\frac{I(D)}{I(G)}$ ratios from Raman spectroscopy indicate that the slip surfaces are coated with nanocrystalline graphite according

to the interpretation of the Raman modes by Ferrari and Robertson (2000). With the obtained $\frac{I(D)}{I(G)}$ ratios we can calculate the size of the nanocrystallites according to the equation from Pimenta et al. (2007)

$$L_a = \frac{560}{E_{\text{laser}}^4} \left(\frac{I(D)}{I(G)} \right)^{-1}, \tag{4}$$

where L_a is the cluster/crystallite size in nm, E_{laser} is the energy (wavelength) of the laser with 2.33 eV (532 nm), and $\frac{I(D)}{I(G)}$ the intensity ratio of D and G peaks. Equation (4) is based on results from Pimenta et al. (2007), which revealed an inversely proportional relationship between the fourth power of E_{laser} and the $\frac{I(D)}{I(G)}$ ratio. For the Arkitsa exposure we calculate a size of $L_a = 35$ nm ($\frac{I(D)}{I(G)} = 0.543$) and for the Schinos exposure $L_a = 24$ nm ($\frac{I(D)}{I(G)} = 0.789$). While Pimenta et al. (2007) calculate with L_a the graphite nanocrystallite size, Ferrari and Robertson (2000) mention L_a as the cluster diameter of carbon aromatic rings. The terminology used by Ferrari and Robertson (2000) for nanocrystalline graphite and amorphous carbon is based on the starting material experiencing disorder. When disordering graphite, $\frac{I(D)}{I(G)}$ will increase with increasing disorder and development of a D peak. With amorphous carbon as the starting material, the development of a D peak and the increase in $\frac{I(D)}{I(G)}$ indicates clustering. Because the D peak arises from aromatic rings, for small L_a the D-mode strength is proportional to the cluster area or diameter (Ferrari and Robertson, 2000).

According to our discussion of possible options for carbon reduction in Section 5.1.1, where the majority of carbon is most likely produced as the outcome of post-seismic, chemical reduction processes, the initially precipitated carbon may be amorphous. Nathan et al. (1974) reported for glass-like carbon a D-peak position at 1340 cm^{-1} and a G-peak position at 1590 cm^{-1}, while Wang et al. (1990) reported a D-peak position at 1347 cm^{-1} and a G-peak position at 1588 cm^{-1}. The band positions from Wang et al. (1990) were obtained with a 515 nm laser on glass-like carbon, which was heat treated at 2000 °C. Wang et al. (1990) also noted that the D-peak position is sensitive to the wavelength of the laser used, exhibiting a band-position shift towards lower wavenumbers with increasing laser wavelength. The reported values from Nathan et al. (1974) and Wang et al. (1990) are in agreement with our measured band positions for Arkitsa (D peak: 1339 cm^{-1}, G peak: 1584 cm^{-1}) and Schinos (D peak: 1344 cm^{-1}, G peak: 1587 cm^{-1}), suggesting that the slip surface coating resembles glass-like carbon. Therefore, instead of the development of nanocrystalline graphite, our results are consistent with the presence of a partly-ordered carbon species exhibiting an electron-bond environment akin to glass-like carbon. The different electron-bond structure may be evidence for the beginning of a clustering process of the aromatic carbon rings (sp^2-clustering), which is likely to have occurred during post-seismic annealing.

High-resolution TEM imaging coupled with electron diffraction suggests that the surface coating is non-crystalline. This interpretation is supported by our EELS analysis, which results in spectra resembling amorphous carbon (Fig. 9). However, although both spectra have a π^* peak, the phase identified here has a more pronounced σ^* region indicating a stronger graphitic order, yet lacking full long-range order as observed in crystalline graphite (Rosenberg et al., 1986). Our spectra resemble those of Stroud et al. (2011), suggested to be indicative of glass-like carbon with sp^2 hybridisation. In addition, heat treatment experiments on non-graphitising carbons by Zhang et al. (2011) produce similar EEL spectra when annealing the initially amorphous material at 600–800 °C. Although the EEL spectra resemble the glass-like carbon phase by Stroud et al. (2011), we will refer to the carbon phase from the fault exposures as partly-hybridised amorphous carbon (PHAC). Impurities of Al, Fe, and Si (Fig. 7) in the PHAC suggest either the concomitant decomposition of silicate phases (e.g., clays) during slip or the influence of hydrothermal fluids percolating along the fault zone, precipitating clay. We suggest that the presence of PHAC demonstrates that amorphous carbon is precipitated during or immediately after slip but undergoes ordering (sp^2-hybridisation) via post-seismic annealing, as demonstrated by Raman spectroscopy and EELS.
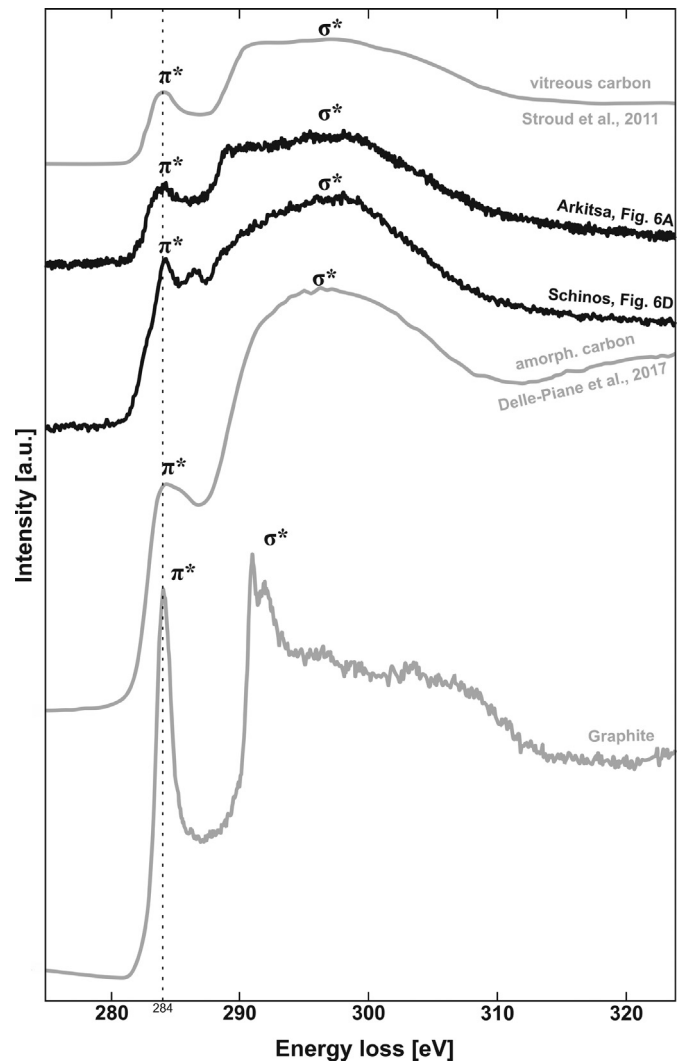

Fig. 9. Comparison of electron energy loss spectra. Calcite decomposition products presented here have a small intensity difference of π^* to σ^* peak. The EEL spectrum from vitreous (glass-like) carbon (Stroud et al., 2011) exhibits a similar σ^*-peak shape compared to the acquired spectra of this study. Reference spectrum of graphite has three weak σ^* peak features which are absent in all other carbon spectra.

5.1.3. Secondary nanograin nucleation

Our nanostructural investigations reveal a close spatial relationship between PHAC and newly formed calcite nanograins (e.g., Fig. 6A). Nucleation of nanograins inside the decomposition product implies a similar chemistry of reactant and product. As discussed in Section 5.1.1, reaction (1) also produces lime, which is highly reactive and can form portlandite (Ca(OH$_2$)) under hydrous conditions via the hydration reaction

$$CaO_{(s)} + H_2O \rightarrow Ca(OH)_{2(s)} \quad (\Delta H^0_{298\,K} = -65\,kJ\,mol^{-1}). \quad (5)$$

In the presence of CO$_2$, portlandite back-reacts to calcite and water by the carbonation reaction

$$Ca(OH)_2 + CO_2 \rightleftharpoons CaCO_3 + H_2O \quad (\Delta H^0_{298\,K} = -93\,kJ\,mol^{-1}). \quad (6)$$
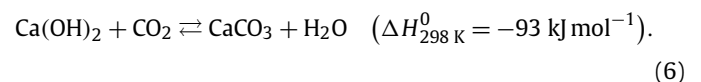
Kudłacz and Rodriguez-Navarro (2014) observed a nucleation-related crystallographic preferred orientation in two sets of portlandite crystals. The angle between the {11-20}$_{portlandite}$ planes was 75°, implying that portlandite developed with a topotactic

relationship of the {11-20}$_{portlandite}$ planes parallel to the {110}$_{CaO}$ planes of lime. The SAED inset of Fig. 6A indicates two preferred orientations with an angle of about 75° (centre to centre) between the {11-20} planes of calcite in our natural samples, supporting our described back-reaction steps from lime, through portlandite, to calcite. In addition, we also observe dislocation-free nanograins away from the slip surface (Fig. 8B). Hence, we suggest that the calcite nanograins of the nanogranular layer in Fig. 5A, 6A, B and 8D are not the outcome of grain-size reduction or plastic deformation processes during slip. We propose that these nanograins are secondary and originate from pseudomorphic growth of calcite after portlandite and portlandite after lime from decarbonation.

5.2. Fault surface evolution during the seismic cycle

The onset of fault slip triggers a variety of inelastic deformation processes. Cleavage fractures in Fig. 3E demonstrate that slip can localise within the first 20 μm inside the fault rock. The localisation shows that the transfer of strain from the slip surface is limited, because the cleavage fractures are concentrated close to the slip surface. Fractures cross-cut the foam nanostructure and produce a nanofabric where grains are trapped between sheet-like fracture planes (Fig. 8A). Fracturing leads to grain-size reduction and produces the primary nanograins, which can fill in surface depressions (Fig. 5B). Shear heating may cause a considerable temperature rise along grain and asperity contacts. The temperature increase or grain fracturing (= mechanical liming) trigger the decarbonation reaction (Eq. (1)), which leads to CO_2 degassing and the production of lime.

During and immediately after fault slip, lime infiltrates cracks and cavities and reacts with the fluids to crystalline portlandite (Eq. (5)). The resulting portlandite crystals back-react with the released CO_2 to form secondary calcite nanograins (Eq. (6)). During the pseudomorphic replacement of portlandite by calcite, the secondary calcite nanograins preserve the crystallographic nucleation relationship from portlandite. Nano-clay precipitates inside the reaction medium either from the fluid or from previously decomposed silicate minerals and may contribute to the fault-mirror appearance. Reduction of carbon can occur by reducing CO_2 with dissolved hydrogen (Eq. (2)) either from the hydrolysis reaction (Eq. (3)) or by water splitting with lime as a catalyst. Subsequent sp^2-hybridisation of the amorphous carbon results in aromatic ring clustering and hence, in a stronger near-field bonding of the carbon. As a result, PHAC is formed.

Graphitisation of carbonaceous materials in active faults may be an important factor for fault reactivation because graphite is characterised by a low friction coefficient of $\mu_{ss} = 0.08$ (Oohashi et al., 2011). Glass-like carbon is a stable, non-graphitising type of carbon, which requires an activation energy of $+215$ kJ mol^{-1} to initiate graphitisation (Saxena and Bragg, 1978; Hokao et al., 2000). The high activation energy would imply that on natural faults graphite can only be found after a considerable energy input to induce graphitisation of glass-like carbon species or when amorphous carbon is initially produced. Kaneki and Hirono (2019) illustrate with their deformation experiments on carbonaceous materials (CMs) that CMs found in natural fault zones can respond differently to imposed deformation. In essence, CMs can decrease in maturity when starting with a mature CM and increase in maturity when deforming a low-maturity CM. Saxena and Bragg (1978) identified three temperature-dependent stages for graphitisation of glass-like carbon: (1) dehydrogenation at <1500 °C, (2) stress relief of the structure at 1500 ≤ 2300 °C, and (3) the onset of graphitisation at >2300 °C. A high temperature treatment of synthetic glass-like carbon can cause graphitisation, suggesting a thermodynamic control of the graphitisation process.

Molecular dynamics simulations of sp^2 carbon-bond self-assembly illustrate that sp^2-clustering from amorphous precursors can commence after 200 picoseconds at ~3200 °C (Powles et al., 2009). This short time span suggests that the sp^2-clustering we observe here takes place immediately after carbon reduction. In addition, the simulations suggest that once sp^2-bonded stable clusters form, breaking these bonds to further rearrange and increase sp^2-ordering may require the need to overcome an additional energy barrier. This behaviour could explain why the PHAC observed here never reached a higher degree of graphitisation, because the energy input was not enough to break the initial, stable carbon clusters. Also, synthetic glass-like carbon displays the often described, entangled, lath-like structure (e.g., Saxena and Bragg, 1978). Although the PHAC observed here lacks the aforementioned nanostructure, it does have the vibrational and electronic properties of glass-like carbon (Fig. 4C and D, Fig. 9).

Because PHAC is formed by chemical precipitation and hybridisation, in contrast to pyrolysis synthesis of glass-like carbon (Powles et al., 2009), we propose that the way the carbon is formed influences the structure of the material while maintaining a similar interatomic bond structure. This suggestion is supported by Powles et al. (2009), who point out that the physical properties of glass-like carbon depend on the formation conditions, the precursor material, and on the annealing conditions. Further research is required to clarify whether the consideration of geological time scales for post-seismic annealing of PHAC at lower temperatures may yield a similar result in gradual graphitisation or whether fault reactivation might contribute to slightly increasing the PHAC maturity by imposing deformation as suggested by Kaneki and Hirono (2019).

5.3. Advances in understanding fault surface evolution

Amorphous carbon has been observed in deformation experiments (Verberne et al., 2014; Spagnuolo et al., 2015; Delle Piane et al., 2017) and its mechanical role has been assessed by Oohashi et al. (2011) and Kaneki and Hirono (2019). Oohashi et al. (2011) measured a friction coefficient for amorphous carbon of $\mu = 0.54$ at the initiation of slip and a low steady-state friction coefficient of $\mu_{ss} = 0.15$ at seismic slip velocities. Di Toro et al. (2011) speculated about fault lubrication by carbonate decomposition products but the present study shows the extent of amorphous coatings. Decarbonation may be an important process for producing a thin fault surface coating and mainly responsible for the low surface roughness by smoothing out surface corrugations. Because the fault surfaces show little variation in the field, our results suggest that the fault planes of both fault exposures are at present covered with the decarbonation and carbon hybridisation products.

Our EEL and Raman spectroscopy results indicate that PHAC has a similar carbon-bonding environment compared to glass-like carbon. Synthetic glass-like carbon has an entangled lath-like structure consisting of ordered carbon sheets while the natural PHAC has no nanostructure. The mechanical properties of glass-like carbon, heat treated at 1000 °C, show a Youngs modulus of $E = 29$ GPa and a shear modulus of $G = 12.5$ GPa (Robertson, 1991). Hokao et al. (2000) report a friction coefficient for glass-like carbon of $\mu = 0.21$ and $\mu = 0.13$ for mixtures of glass-like carbon with graphite. However, as the structure of the PHAC is different from synthetic glass-like carbon, we suggest that mechanical properties of the synthetic material may not fully reflect the mechanical behaviour of the carbon phase reported here. Because little is known about the deformation of various crystalline and non-crystalline carbon phases, further experimental investigations are warranted.

While previous research focused mainly on mechanisms of grain size reduction (Sammis and Ben-Zion, 2008; Siman-Tov et al., 2013), our results highlight the importance of decarbonation and back-reactions as part of the overall fault deformation and healing behaviour. In contrast to Siman-Tov et al. (2013), we do not observe small grains evolving from fracturing long, twin-derived beams of calcite. However, our results indicate that, for the natural carbonate faults studied here, a nanogranular coating is not the only feature producing a fault mirror surface, similar to results of Fondriest et al. (2013). For example, the Schinos fault exposure illustrates that MMSs can contain no coating of calcite nanograins (Fig. 7C, E and F). Instead, MSS are produced by the interplay of grain-size reduction, decarbonation, back-reactions, and annealing. The present study does not exclude crystal-plastic or brittle deformation as an important grain-size reduction mechanism in fault gouges to form primary nanograins. Instead, we demonstrate that grain-size reduction alone may not be the governing mechanism to form a fault mirror surface. The formation of an amorphous phase with low viscosity during deformation could explain the low friction, stable, near-steady-state behaviour after the onset of weakening observed by Han et al. (2007a and 2007b), as well as the increase in friction coefficient via re-carbonation and carbon hybridisation after displacement stopped (Spagnuolo et al., 2015). The chemical reactions revealed here suggest that a succession of healing reactions take place after fault slip ceases.

6. Conclusions

We conclude that decarbonation of calcite and the subsequent reaction of the decarbonation products produces fault mirror surfaces. The decarbonation process itself may be a major co-seismic fault weakening factor and, fault slip is facilitated on a decarbonation-product glide film. Frictional behaviour during slip may be dictated by lubrication of low viscosity (amorphous) calcium oxide and (amorphous) carbon. Occasional precipitation of clay inside the decarbonation products may contribute to decreasing surface roughness. Post-seismic hybridisation produces partly-hybridised amorphous carbon and connects footwall with hanging wall. Ultimately, post-seismic carbonation of portlandite produces new, secondary nano-sized calcite crystals <50 nm by pseudomorphic replacement, and this carbonation facilitates fault healing.

Acknowledgements

Appendix A. Supplementary material

Supplementary material related to this article can be found online at https://doi.org/10.1016/j.epsl.2019.115886.

References

Ambraseys, N.N., Jackson, J.A., 1990. Seismicity and associated strain of central Greece between 1890 and 1988. Geophys. J. Int. 101, 663–708. https://doi.org/10.1111/j.1365-246X.1990.tb05577.x.

Bullock, R.J., De Paola, N., Holdsworth, R.E., Trabucho-Alexandre, J., 2014. Lithological controls on the deformation mechanisms operating within carbonate-hosted faults during the seismic cycle. J. Struct. Geol. 58, 22–24. https://doi.org/10.1016/j.jsg.2013.10.008.

Collettini, C., Viti, C., Tesei, T., Mollo, S., 2013. Thermal decomposition along natural carbonate faults during earthquakes. Geology 41, 927–930. https://doi.org/10.1130/G34421.1.

Collettini, C., Carpenter, B.M., Viti, C., Cruciani, F., Mollo, S., Tesei, T., Trippetta, F., Valoroso, L., Chiaraluce, L., 2014. Fault structure and slip localization in carbonate-bearing normal faults: an example from the Northern Apennines of Italy. J. Struct. Geol. 67, 154–166. https://doi.org/10.1016/j.jsg.2014.07.017.

Collier, R.E., Pantosti, D., D'addezio, G., De Martini, P.M., Masana, E., Sakellariou, D., 1998. Paleoseismicity of the 1981 Corinth earthquake fault: seismic contribution to extensional strain in central Greece and implications for seismic hazard. J. Geophys. Res., Solid Earth 103, 30001–30019. https://doi.org/10.1029/98JB02643.

De Paola, N., Hirose, T., Mitchell, T., Di Toro, G., Viti, C., Shimamoto, T., 2011. Fault lubrication and earthquake propagation in thermally unstable rocks. Geology 39, 35–38. https://doi.org/10.1130/G31398.1.

De Paola, N., Holdsworth, R.E., Viti, C., Collettini, C., Bullock, R., 2015. Can grain size sensitive flow lubricate faults during the initial stages of earthquake propagation? Earth Planet. Sci. Lett. 431, 48–58. https://doi.org/10.1016/j.epsl.2015.09.002.

Delle Piane, C., Piazolo, S., Timms, N.E., Luzin, V., Saunders, M., Bourdet, J., Giwelli, A., Ben Clennell, M., Kong, C., Rickard, W.D., 2017. Generation of amorphous carbon and crystallographic texture during low-temperature subseismic slip in calcite fault gouge. Geology 46, 163–166. https://doi.org/10.1130/G39584.1.

Demurtas, M., Smith, S.A., Prior, D.J., Spagnuolo, E., Di Toro, G., 2019. Development of crystallographic preferred orientation during cataclasis in low-temperature carbonate fault gouge. J. Struct. Geol. 126, 37–50. https://doi.org/10.1016/j.jsg.2019.04.015.

Di Toro, G., Goldsby, D.L., Tullis, T.E., 2004. Friction falls towards zero in quartz rock as slip velocity approaches seismic rates. Nature 427, 436. https://doi.org/10.1038/nature02249.

Di Toro, G., Han, R., Hirose, T., De Paola, N., Nielsen, S., Mizoguchi, K., Ferri, F., Cocco, M., Shimamoto, T., 2011. Fault lubrication during earthquakes. Nature 471, 494. https://doi.org/10.1038/nature09838.

Ferrari, A.C., Robertson, J., 2000. Interpretation of Raman spectra of disordered and amorphous carbon. Phys. Rev. B 61, 14095. https://doi.org/10.1103/PhysRevB.61.14095.

Fondriest, M., Smith, S.A., Candela, T., Nielsen, S.B., Mair, K., Di Toro, G., 2013. Mirror-like faults and power dissipation during earthquakes. Geology 41, 1175–1178. https://doi.org/10.1130/G34641.1.

Ganas, A., Roberts, G.P., Memou, T., 1998. Segment boundaries, the 1894 ruptures and strain patterns along the Atalanti Fault, central Greece. J. Geodyn. 26, 461–486. https://doi.org/10.1016/S0264-3707(97)00066-5.

Ganas, A., Sokos, E., Agalos, A., Leontakianakos, G., Pavlides, S., 2006. Coulomb stress triggering of earthquakes along the Atalanti Fault, central Greece: two April 1894 M6 events and stress change patterns. Tectonophysics 420, 357–369. https://doi.org/10.1016/j.tecto.2006.03.028.

Gevantman, L., 2000. Solubility of selected gases in water. Nitric Oxide 308, 10–14.

Goldberg, R., Siman-Tov, S., Emmanuel, S., 2016. Weathering resistance of carbonate fault mirrors promotes rupture localization. Geophys. Res. Lett. 43, 3105–3111. https://doi.org/10.1002/2016GL067788.

Green, H.W., Shi, F., Bozhilov, K., Xia, G., Reches, a Z., 2015. Phase transformation and nanometric flow cause extreme weakening during fault slip. Nat. Geosci. 8, 484. https://doi.org/10.1038/ngeo2436.

Han, R., Shimamoto, T., Hirose, T., Ree, J., Ando, J., 2007a. Ultralow friction of carbonate faults caused by thermal decomposition. Science 316, 878–881. https://doi.org/10.1126/science.1139763.

Han, R., Shimamoto, T., Ando, J., Ree, J.-H., 2007b. Seismic slip record in carbonate-bearing fault zones: an insight from high-velocity friction experiments on siderite gouge. Geology 35, 1131–1134. https://doi.org/10.1130/G24106A.1.

Han, R., Hirose, T., Shimamoto, T., 2010. Strong velocity weakening and powder lubrication of simulated carbonate faults at seismic slip rates. J. Geophys. Res., Solid Earth 115. https://doi.org/10.1029/2008JB006136.

Hirose, T., Mizoguchi, K., Shimamoto, T., 2012. Wear processes in rocks at slow to high slip rates. J. Struct. Geol. 38, 102–116. https://doi.org/10.1016/j.jsg.2011.12.007.

Hokao, M., Hironaka, S., Suda, Y., Yamamoto, Y., 2000. Friction and wear properties of graphite/glassy carbon composites. Wear 237, 54–62. https://doi.org/10.1016/S0043-1648(99)00306-3.

Jackson, J., McKenzie, D., 1999. A hectare of fresh striations on the Arkitsa fault, central Greece. J. Struct. Geol. 21, 1–6. https://doi.org/10.1016/S0191-8141(98)00091-1.

Johnson, J.W., Oelkers, E.H., Helgeson, H.C., 1992. SUPCRT92: a software package for calculating the standard molal thermodynamic properties of minerals, gases, aqueous species, and reactions from 1 to 5000 bar and 0 to 1000 °C. Comput. Geosci. 18, 899–947. https://doi.org/10.1016/0098-3004(92)90029-Q.

Jones, R.R., Kokkalas, S., McCaffrey, K., 2009. Quantitative analysis and visualization of nonplanar fault surfaces using terrestrial laser scanning (LIDAR)—the Arkitsa fault, central Greece, as a case study. Geosphere 5, 465–482. https://doi.org/10.1130/GES00216.1.

Kaneki, S., Hirono, T., 2019. Diagenetic and shear-induced transitions of frictional strength of carbon-bearing faults and their implications for earthquake rupture dynamics in subduction zones. Sci. Rep. 9, 7884. https://doi.org/10.1038/s41598-019-44307-y.

Kaplanis, A., Koukouvelas, I., Xypolias, P., Kokkalas, S., 2013. Kinematics and ophiolite obduction in the Gerania and Helicon Mountains, central Greece. Tectonophysics 595, 215–234. https://doi.org/10.1016/j.tecto.2012.07.014.

Kirkpatrick, J.D., Rowe, C.D., White, J.C., Brodsky, E.E., 2013. Silica gel formation during fault slip: evidence from the rock record. Geology 41, 1015–1018. https://doi.org/10.1130/G34483.1.

Kokkalas, S., Jones, R.R., McCaffrey, K., Clegg, P., 2007. Quantitative fault analysis at Arkitsa, central Greece, using terrestrial laser-scanning (LiDAR). Bul. Geol. Soc. Greece 37, 1–14.

Kudłacz, K., Rodriguez-Navarro, C., 2014. The mechanism of vapor phase hydration of calcium oxide: implications for CO_2 capture. Environ. Sci. Technol. 48, 12411–12418. https://doi.org/10.1021/es5034662.

Martinelli, G., Plescia, P., 2004. Mechanochemical dissociation of calcium carbonate: laboratory data and relation to natural emissions of CO_2. Phys. Earth Planet. Inter. 142, 205–214. https://doi.org/10.1016/j.pepi.2003.12.009.

Milesi, V., Guyot, F., Brunet, F., Richard, L., Recham, N., Benedetti, M., Dairou, J., Prinzhofer, A., 2015. Formation of CO_2, H_2 and condensed carbon from siderite dissolution in the 200–300 °C range and at 50 MPa. Geochim. Cosmochim. Acta 154, 201–211. https://doi.org/10.1016/j.gca.2015.01.015.

Nathan, M.I., Smith Jr, J.E., Tu, K.N., 1974. Raman spectra of glassy carbon. J. Appl. Phys. 45, 2370. https://doi.org/10.1063/1.1663599.

Oohashi, K., Hirose, T., Shimamoto, T., 2011. Shear-induced graphitization of carbonaceous materials during seismic fault motion: experiments and possible implications for fault mechanics. J. Struct. Geol. 33, 1122–1134. https://doi.org/10.1016/j.jsg.2011.01.007.

Oohashi, K., Han, R., Hirose, T., Shimamoto, T., Omura, K., Matsuda, T., 2014. Carbon-forming reactions under a reducing atmosphere during seismic fault slip. Geology 42, 787–790. https://doi.org/10.1130/G35703.1.

Pec, M., Stünitz, H., Heilbronner, R., Drury, M., de Capitani, C., 2012. Origin of pseudotachylites in slow creep experiments. Earth Planet. Sci. Lett. 355, 299–310. https://doi.org/10.1016/j.epsl.2012.09.004.

Pimenta, M.A., Dresselhaus, G., Dresselhaus, M.S., Cancado, L.G., Jorio, A., Saito, R., 2007. Studying disorder in graphite-based systems by Raman spectroscopy. Phys. Chem. Chem. Phys. 9, 1276–1290. https://doi.org/10.1039/B613962K.

Pluymakers, A., Røyne, A., 2017. Nanograin formation and reaction-induced fracturing due to decarbonation: implications for the microstructures of fault mirrors. Earth Planet. Sci. Lett. 476, 59–68. https://doi.org/10.1016/j.epsl.2017.08.001.

Powles, R.C., Marks, N.A., Lau, D., 2009. Self-assembly of sp^2-bonded carbon nanostructures from amorphous precursors. Phys. Rev. B 79, 075430. https://doi.org/10.1103/PhysRevB.79.075430.

Roberts, S., Jackson, J., 1991. Active Normal Faulting in Central Greece: An Overview. Special Publications, vol. 56. Geological Society, London, pp. 125–142.

Robertson, J., 1991. Hard amorphous (diamond-like) carbons. Prog. Solid State Chem. 21, 199–333. https://doi.org/10.1016/0079-6786(91)90002-H.

Rodriguez-Navarro, C., Ruiz-Agudo, E., Luque, A., Rodriguez-Navarro, A.B., Ortega-Huertas, M., 2009. Thermal decomposition of calcite: mechanisms of formation and textural evolution of CaO nanocrystals. Am. Mineral. 94, 578–593. https://doi.org/10.2138/am.2009.3021.

Rosenberg, R.A., Love, P.J., Rehn, V., 1986. Polarization-dependent C (K) near-edge x-ray-absorption fine structure of graphite. Phys. Rev. B 33, 4034. https://doi.org/10.1103/PhysRevB.33.4034.

Ruiz-Agudo, E., Kudłacz, K., Putnis, C.V., Putnis, A., Rodriguez-Navarro, C., 2013. Dissolution and carbonation of portlandite [Ca(OH)$_2$] single crystals. Environ. Sci. Technol. 47, 11342–11349. https://doi.org/10.1021/es402061c.

Sammis, C.G., Ben-Zion, Y., 2008. Mechanics of grain-size reduction in fault zones. J. Geophys. Res., Solid Earth 113. https://doi.org/10.1029/2006JB004892.

Saxena, R.R., Bragg, R.H., 1978. Kinetics of graphitization in glassy carbon. Carbon 16, 373–376. https://doi.org/10.1016/0008-6223(78)90077-5.

Scholz, C.H., 1998. Earthquakes and friction laws. Nature 391, 37. https://doi.org/10.1038/34097.

Siman-Tov, S., Aharonov, E., Sagy, A., Emmanuel, S., 2013. Nanograins form carbonate fault mirrors. Geology 41, 703–706. https://doi.org/10.1130/G34087.1.

Smeraglia, L., Bettucci, A., Billi, A., Carminati, E., Cavallo, A., Di Toro, G., Natali, M., Passeri, D., Rossi, M., Spagnuolo, E., 2017. Microstructural evidence for seismic and aseismic slips along clay-bearing, carbonate faults. J. Geophys. Res., Solid Earth 122, 3895–3915. https://doi.org/10.1002/2017JB014042.

Smith, S., Di Toro, G., Kim, S., Ree, J., Nielsen, S., Billi, A., Spiess, R., 2013. Coseismic recrystallization during shallow earthquake slip. Geology 41, 63–66. https://doi.org/10.1130/G33588.1.

Spagnuolo, E., Plümper, O., Violay, M., Cavallo, A., Di Toro, G., 2015. Fast-moving dislocations trigger flash weakening in carbonate-bearing faults during earthquakes. Sci. Rep. 5, 16112. https://doi.org/10.1038/srep16112.

Stroud, R.M., Chisholm, M.F., Heck, P.R., Alexander, C.M., Nittler, L.R., 2011. Supernova shock-wave-induced co-formation of glassy carbon and nanodiamond. Astrophys. J. Lett. 738, L27. https://doi.org/10.1088/2041-8205/738/2/L27.

Tisato, N., Di Toro, G., De Rossi, N., Quaresimin, M., Candela, T., 2012. Experimental investigation of flash weakening in limestone. J. Struct. Geol. 38, 183–199. https://doi.org/10.1016/j.jsg.2011.11.017.

Toy, V.G., Mitchell, T.M., Druiventak, A., Wirth, R., 2015. Crystallographic preferred orientations may develop in nanocrystalline materials on fault planes due to surface energy interactions. Geochem. Geophys. Geosyst. 16, 2549–2563. https://doi.org/10.1002/2015GC005857.

Verberne, B.A., Spiers, C.J., Niemeijer, A.R., De Bresser, J., De Winter, D., Plümper, O., 2014. Frictional properties and microstructure of calcite-rich fault gouges sheared at sub-seismic sliding velocities. Pure Appl. Geophys. 171, 2617–2640. https://doi.org/10.1007/s00024-013-0760-0.

Vigano, A., Tumiati, S., Recchia, S., Martin, S., Marelli, M., Rigon, R., 2011. Carbonate pseudotachylytes: evidence for seismic faulting along carbonate faults. Terra Nova 23, 187–194. https://doi.org/10.1111/j.1365-3121.2011.00997.x.

Wang, Y., Alsmeyer, D.C., McCreery, R.L., 1990. Raman spectroscopy of carbon materials: structural basis of observed spectra. Chem. Mater. 2, 557–563. https://doi.org/10.1021/cm00011a018.

Wojdyr, M., 2010. Fityk: a general purpose peak fitting program. J. Appl. Crystallogr. 43, 1126–1128. https://doi.org/10.1107/S0021889810030499.

Yund, R.A., Blanpied, M.L., Tullis, T.E., Weeks, J.D., 1990. Amorphous material in high strain experimental fault gouges. J. Geophys. Res., Solid Earth 95, 15589–15602. https://doi.org/10.1029/jb095ib10p15589.

Zhang, Z., Brydson, R., Aslam, Z., Reddy, S., Brown, A., Westwood, A., Rand, B., 2011. Investigating the structure of non-graphitising carbons using electron energy loss spectroscopy in the transmission electron microscope. Carbon. 49, 5049–5063. https://doi.org/10.1016/j.carbon.2011.07.023.